Experimental and numerical study of the influence of small geometrical modifications on the dynamics of swirling flows

By J. Dombard, T. Poinsot†‡, V. Moureau¶, N. Savary‖, G. Staffelbach†† AND V. Bodoc‡‡

This report presents a joint experimental and numerical study of the non-reacting flow in a swirler where small geometrical variations are imposed on a row of holes. Simulation results are compared to experimental data in terms of mean and Root Mean Square (RMS) velocity fields as well as in terms of unsteady activity (e.g. hydrodynamic modes such as the Precessing Vortex Core (PVC), which is characteristic of such flows). Results demonstrate that Large-Eddy Simulation (LES) captures the mean and RMS fields very well; LES can also predict the fact that, in one case, two hydrodynamic modes are identified experimentally, and that one of them disappears when the row of holes is displaced.

1. Introduction

Swirling flows are commonly used in gas turbines to stabilize combustion. The first advantage of swirl is that the rotation imposed on the flow creates a large Central Recirculation Zone (CRZ), which is essential for flame stabilization (Gupta *et al.* 1984; El-Asrag & Menon 2007; Poinsot & Veynante 2011). On the other hand, it has been long recognized (Billant *et al.* 1998; Roux *et al.* 2005) that swirling flows are often submitted to absolute instability (Ho & Huerre 1984), leading to strongly unstable hydrodynamic modes that can compromise the overall stability of the combustion chamber and cause combustion instability when they couple with acoustic modes (Huang & Yang 2004; Staffelbach *et al.* 2009). The present design of swirlers used in combustion chambers relies on complex geometrical shapes, often based on multiple swirler passages and subject to permanent optimization because the swirler controls a large part of the chamber performances: flame stabilization, mixing between fuel and air, flame stability, ignition capacities, etc. In this context, being able to optimize swirlers numerically has become a major issue because this optimization would be too expensive experimentally. This optimization essentially requires simulating three types of problems: (1) obtaining the correct velocity fields, (2) predicting the correct pressure losses and (3) capturing hydrodynamic modes to limit their amplitudes.

One of the specificities of swirling flows is that all three problem types are sensitive to small geometrical changes. Experimentalists know that a minor design variation in a swirler can cause a strong flow change such that hysteresis and bifurcations are common

† Université de Toulouse; INPT, UPS; IMFT (Institut de Mécanique des Fluides de Toulouse); Allée Camille Soula, F-31400 Toulouse, France
‡ CNRS; IMFT; F-31400 Toulouse, France
¶ CORIA, Rouen, France
‖ TURBOMECA, Bordes, France
†† CERFACS, 31057 Toulouse, France
‡‡ ONERA-CT, 2 avenue Edmond-Belin, 31055 Toulouse Cedex 04, France

features in many swirling flows (Dellenback *et al.* 1988; Vanierschot & den Bulck 2007). Vanierschot *et al* show that four different mean flow patterns can be obtained by small variations of the swirl number and that the transition between these four states depends on the method used to vary swirl: decreasing or increasing swirl number leads to different transitions. These transitions are observed on the velocity field but also on the pressure losses, which are another important characteristic of the flow. The study of Vanierschot *et al* focused on the mean flow patterns but the instability modes can also change for very small modifications of geometry or of flow parameters, leading to the appearance of strong hydrodynamic modes for certain regimes.

The simulation of swirling flows relies on Reynolds-Averaged Navier-Stokes (RANS) and/or Large-Eddy Simulation (LES) techniques. LES (Large Eddy Simulation) has become a reference method for swirling flows in the last ten years (Huang *et al.* 2003; Mare *et al.* 2004; Huang *et al.* 2006; Roux *et al.* 2005; Moureau *et al.* 2011). The main reason for this fast development is that LES has demonstrated superior performances compared to RANS for swirling flows that are dominated by large unsteady structures and a strong mean rotation. Recent results suggest however that LES may be adequate for Types 1 (velocity fields) and III (unstable modes) problems but may have difficulties in predicting pressure losses.

The objective of the present work was to consider a swirler installed at ONERA Toulouse and compute it using various LES and RANS codes to address Type 1 to 3 problems. For this swirler, multiple small variations of the geometry have been tested: two specific cases called cA and cI (cA and cI refer to configuration A and I, respectively) are retained here because one case produces more unstable modes than the other, even though the design difference between the two is very small (a few holes are displaced by a few millimeters in the 4^{th} passage). This exercise is performed for a cold flow case, comparing experimental (PIV) and numerical results. Mesh independency is studied. The unstable mode observed for such a swirler is usually a Precessing Vortex Core (PVC) (Syred 2006) ; we will also compare the results of the LES and of the experiment using velocity spectra obtained by hot-wire anemometry in the CRZ to characterize this PVC.

The configuration is described in Section 2. The experimental and numerical set up are presented in Section 2 while Section 3 describes the Computational Fluid Dynamics (CFD) solvers used for the study. Section 4.1 presents a comparison of mean velocity data obtained by PIV and LES for configuration cA. The differences between cA and cI obtained experimentally and numerically are discussed in Section 4.2. Section 4.3 presents the effect of the mesh size on the results. Pressure losses are discussed in Section 4.4. Uncertainty quantification of the CRZ position is shown in Section 4.5. Finally, the flow dynamics are studied in Section 4.6, where the velocity spectra obtained for the A and I cases are compared both experimentally and numerically.

2. Configurations

In this paper, two geometrical variations of the same swirler (called A and I) are compared. The parent configuration consists in a radial swirler with four passages of air, as shown in Figure 1. It is composed of twelve purge holes, twelve primary and secondary vanes (referred to as primary and secondary swirlers, respectively), a venturi, a flare and a given number of flare-cooling slots which will be referred to as peripheral

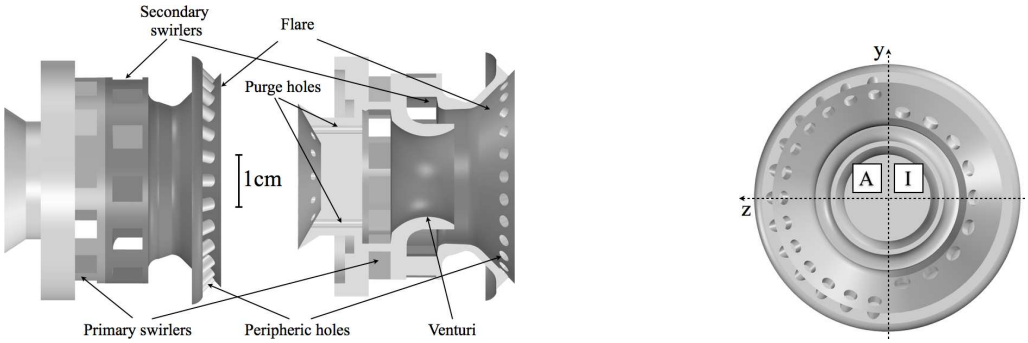

FIGURE 1. Left: computer-aided design of the swirler A. The nomenclature follows that of Wang *et al.* (2007). The purge holes have a diameter of 1.5 mm. Right: front view of the flare of configurations A (left) and I (right). The two configurations differ only by the number, position and size of the peripheral holes.

Config.	Number	Diameter [mm]	Perforation radius [mm]	Equivalent section S_{sw} [mm^2]
A	26	2.4	18	117.6
I	12	2.85	15	114.8

TABLE 1. Characteristics of the peripheral holes of both configurations

holes. The primary and secondary vanes are co-rotative and counter-clockwise looking from the downstream side in the axial direction.

The sole differences between cA and cI are the number, diameter and perforation radius (*i.e* the distance from the centerline) of the peripheral holes, as shown in Figure 1 right and summarized in Table 1. The difference in the number and diameter of the peripheral holes between cA and cI is expected to have a limited impact on the flow since the equivalent section is similar. Moreover, their center's positions are axisymmetric so that no unbalance of the mass-flow rate is expected. However, the perforation radius might have a large effect on the flow circulation in the primary area since it may change the recirculation bubble shape. Consequently, these geometrical differences, although minor in regards to the complexity of the swirlers, may affect the flow dynamics.

The experimental and computational setup are as similar as possible (Figure 2). The only difference is the presence of a small coflow in the numerical setup for numerical stability reasons. The swirler is fed by a plenum, which allows accurate control of the inlet mass-flow rate. The swirler blows directly into the atmosphere to allow easy access for the PIV measurements and to avoid acoustic reflections that may contaminate pressure spectra close to the swirler.

The positions of the experimental measurement lines are shown in Figure 2(b). The x-axis is aligned with the swirler centerline and $x = 0$ corresponds to the swirler's exit. Two experimental methods were used:

- Gas velocity measurements with hot-wire anemometry were performed inside the swirler at probe P1. The instantaneous velocity signal measured by the hot-wire probe is denoted u_{hw}.
- PIV measurements of the velocity flow field were made at three transverse cuts along the streamwise direction at $x = 5.5$, 15 and 30 mm and one longitudinal cut at $z = 0$.

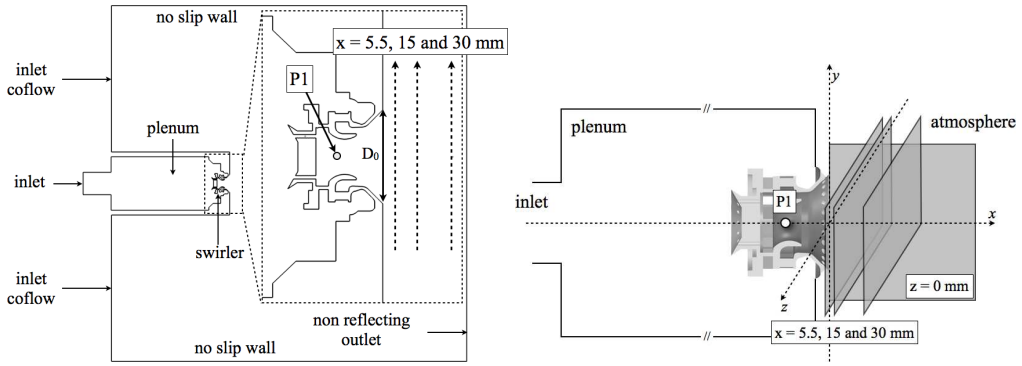

(a) Numerical setup (b) Experimental setup

FIGURE 2. Left: Cut at $Z = 0$ of the configuration (overview plus a zoom around the swirler). The vertical dashed lines give the location of the transverse cuts used for velocity profiles. Right: Schematic of the experimental setup. The three transverse ($x = \{5.5; 10; 30\}$ mm) and single longitudinal ($z = 0$) PIV planes are higlighted. In both figures, the black circle indicates the location ($(x, y, z) = (-20, 0, 0)$ mm) of the probe, denoted P1, where the velocity signal is recorded from the LES and experiment.

Pure air is injected at $T = 282$ K at pressure $P_0 = 101325$ Pa, yielding a density of $\rho = 1.251$ kg.m^{-3}. For a meaningful comparison between cA and cI, the same mass flow rate $\dot{m} = 32.1$ g.s^{-1} is supplied for both configurations. The bulk velocity $U_b = \dot{m}/(\rho S_{in}) = 13.2$ m.s^{-1}, where $S_{in} = 1.951 \cdot 10^{-3}$ m^2 is the inlet's surface. The flare downstream diameter, $D_0 = 40$ mm (*cf.* zoom in Figure 2(a)), and the bulk velocity are employed as the reference length and velocity, respectively. The corresponding Reynolds number is Re $\sim 3.9 \cdot 10^4$. The reference time $t_{ref} = D_0/U_b$ is 3 ms. The "local" swirl number is defined as

$$S = \frac{\int_0^{R(x)} \rho u_x u_\theta r^2 dr}{R(x) \int_0^{R(x)} \rho u_x^2 r dr}, \tag{2.1}$$

where u_θ and $R(x)$ are the tangential velocity and radius to the closest wall perpendicular to the axis inside the injector, respectively. The variation of the time-averaged swirl number computed for cA and cI along the x-axis is shown in Figure 3. Swirl is larger than 0.5 in the whole injector. It increases at the tip of the venturi, where the angular momentum flux grows due to the co-rotating secondary swirler exit and then declines. Swirl-number profiles are similar between cA and cI.

3. Numerical solvers, boundary conditions and grid

Multiple RANS and LES solvers were used in the present work. AVBP is a compressible cell-vertex code for turbulent reacting two phase flows, on both structured and unstructured hybrid meshes (Granet *et al.* 2012; Poinsot & Veynante 2011; Roux *et al.* 2005; Selle *et al.* 2004; Wolf *et al.* 2012). It uses a third-order in space and time scheme called TTGC (Colin & Rudgyard 2000). Subgrid-scale turbulence is accounted for with the WALE model (Nicoud & Ducros 1999). The outlet pressure and the mass-flow rate are imposed using the NSCBC formulation (Poinsot & Lele 1992; Granet *et al.* 2010). No-slip adiabatic conditions are applied at all walls. YALES2 is an incompressible LES solver (Moureau *et al.* 2011) using hybrid meshes. No slip boundary conditions are used on all walls and the dynamic Smagorinsky model is used for turbulence modeling. Since

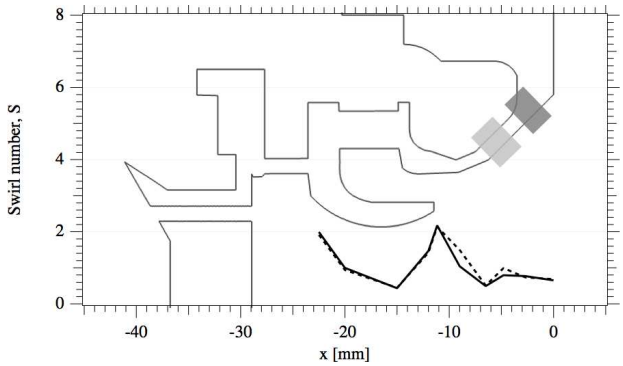

FIGURE 3. Swirl number profiles along the injector A (-) and I (- - - - -). The half cut in the xOy-plane of the swirler is drawn in background. Dark and light grey rectangles point the positions of the peripheral holes for cA and cI, respectively.

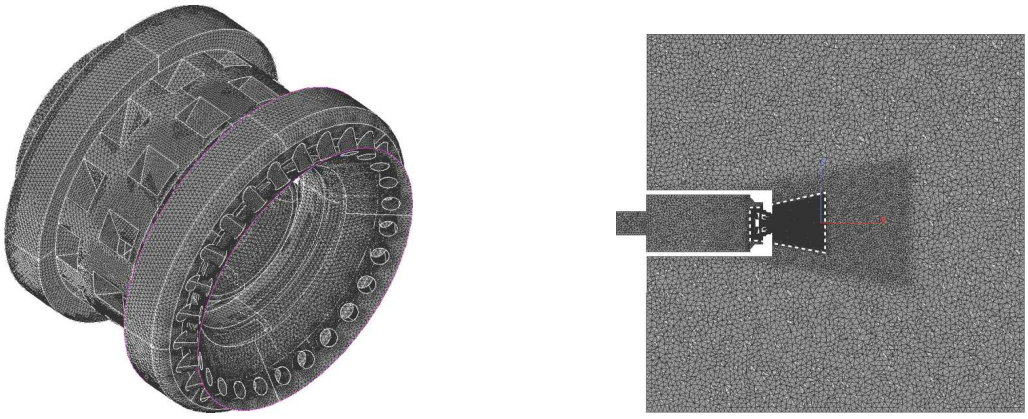

(a) (b)

FIGURE 4. Baseline mesh of config A. Figure 4(a): isometric view of the swirler. Figure 4(b): overview of the domain. White dashes highlight the region where the mesh is refined in the fine mesh.

the solver is incompressible, the only boundary condition is the total mass flow rate. Fluent and N3S, an in-house code of Safran, were used for RANS computations. All RANS solvers used wall-law formulations. Turbulence is accounted for with the standard (Launder & Jones 1972) and realizable (Shih *et al.* 1995) $k-\varepsilon$ model in N3S and Fluent, respectively.

For each configuration, all codes were run on two unstructured full-tetraedral meshes called "baseline" (8.6 M cells) and "fine" (43.7 M cells). Both the plenum and a portion of the surroundings of the swirler are meshed, as shown in Figure 4(b). At least ten points are found across the air passages for the baseline mesh, even in the peripheral holes (yielding a local mesh size of $1.5 \cdot 10^{-4}$ m). In the fine mesh (not shown here), the cell resolution in the region delimited by white dashes in Figure 4(b) is doubled in each direction. However, the plenum and atmosphere have the same grid resolution in both meshes so that the baseline mesh contains 1.5 million nodes and 8.6 million cells whereas the fine mesh is constituted of 7.5 and 43.7 million nodes and cells, respectively. The same grid spacing is used for configurations A and I.

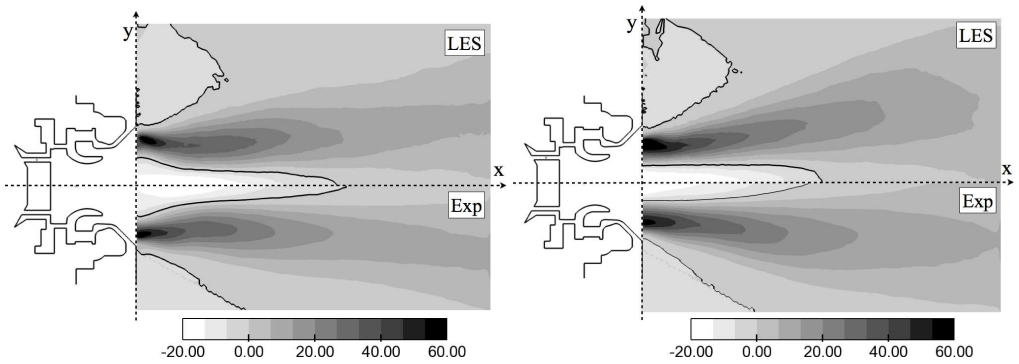

(a) Configuration A (b) Configuration I

FIGURE 5. Comparison at z = 0 mm of time-averaged AVBP (top) and PIV (bottom) axial velocities for configurations A (left) and I (right). Zero-velocity isoline in solid line.

For the LES codes, all flow quantities are time-averaged during 13.5 t_{ref} (41 ms) where $t_{ref} = D_0/U_b$. It has been checked that time-averaged quantities were converged.

4. Results and discussion

4.1. *Comparison of mean flows for simulations and experiment*

First, a qualitative comparison is conducted between time-averaged axial velocities and PIV measurements in xOy planes for configuration A (Figure 5). The axial velocity is coherent with the high swirl number used in the present configurations. Since the swirl number is large (between one half and two, *cf.* Figure 3), the static pressure just outside the swirler becomes low enough to induce a recirculation region (Lefebvre 1999), highlighted in Figure 5 by a solid line. The axial velocity field is maximum close to the swirler exit and then decreases when the jet widens. Moving the peripheral holes changes the jet angle and the length of the recirculation region. Whereas the jet widens monotically for cI, the topology of the flow is slightly different for cA: the jet is wider at the exit of the swirler than cI, narrows rapidly due to the peripheral holes and then widens again. Moreover, the recirculation zone is longer in cA ($L/D_0 = 1.67$) than in cI ($L/D_0 = 1.48$). LES and PIV measurements agree fairly well. Both the position of the stagnation point and the jet angle are captured.

Mean axial and azimuthal velocity profiles along the y-axis are shown in Figure 6 for configuration cA (cI provides similar levels of agreement between simulations and PIV data) and for four codes: AVBP, YALES2, FLUENT and N3S. The turbulent kinetic energy is also displayed (RANS codes cannot provide RMS values of velocities). Only one transverse cut ($x = 5.5$ mm) is shown for the sake of compactness. Conclusions are similar for the other cuts. Both LES and RANS codes have a good agreement with the experiment, even for the turbulent kinetic energy.

4.2. *Comparison between configurations cA and cI*

A comparison between cA and cI is given in Figure 7 with the mean and RMS axial velocity profiles for AVBP results and experimental data only. Conclusions are similar for transverse and azimuthal velocity profiles (not shown).

The effect of the peripheral holes fades rapidly and velocity profiles for cA and cI are almost identical at $x = 30$ mm, less than one reference diameter D_0. LES captures

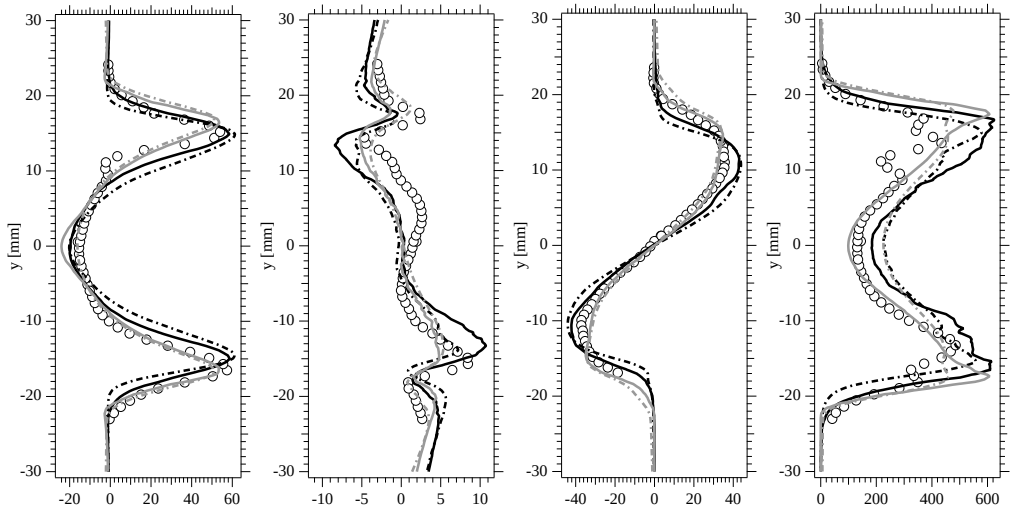

FIGURE 6. From left to right: Mean axial, radial velocity, tangential velocity and turbulent kinetic energy profiles for configuration cA at $x = 5.5$ mm. LES solvers are in black: AVBP (——) and YALES2 (–·–·–) whereas RANS solvers are in gray: FLUENT(——) and N3S (–·–·–) and PIV in symbol (◯).

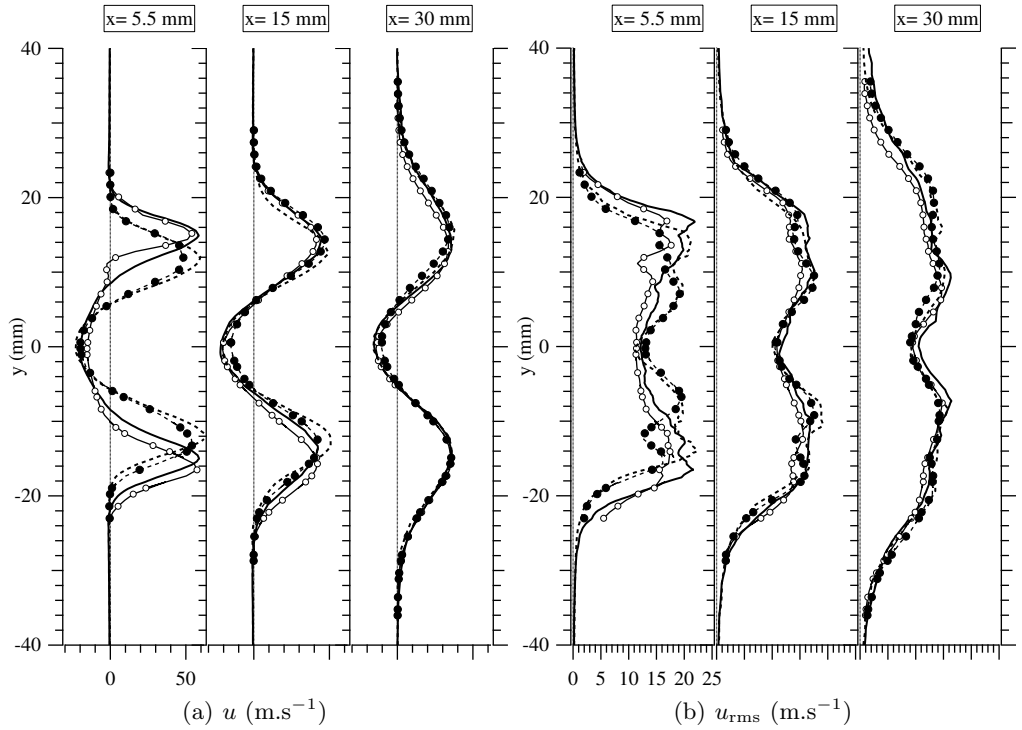

FIGURE 7. Mean (left) and RMS (right) axial velocity profiles for LES with AVBP of configuration A (——) and I (– – – –). PIV of configuration A (—◯—) and I (– – •– –).

the variations of the velocity profiles from cA and cI and reproduces PIV results: the spreading rate of the jet is smaller for cI than for cA close to the swirler exit but they are similar further downstream ($x = 30mm$) where the effect of the peripheral holes has clearly disappeared. This is not unexpected because the differences between cA and cI are small.

Axial velocity fluctuations are shown in Figure 7(b). Overall, the turbulence intensity is relatively high: in the first measurement plane, it is of the order of 50 percent. This is consistent with the Reynolds number (Re$\sim 3.9 \cdot 10^4$) and the usual values found in swirling flows which are dominated by a strong hydrodynamic mode (Precessing Vortex Core) which will be discussed in Section 4.6 (Roux *et al.* 2005). LES and experiment also agree very well for RMS velocities, except in the shear layer at $x = 5.5$ mm, where LES moderately overpredicts the axial velocity fluctuations. That may be due to a lack of resolution of the PIV in the shear layer.

4.3. *Impact of mesh refinement on the velocity profiles*

Mesh requirements for LES of swirling flows are still an open question: in the swirler itself, meshing each air passage precisely would require billions of points especially if a wall resolved LES is performed. At the same time, multiple LES papers have recently shown that the velocity profiles downstream of the swirler were only weakly dependent on the details of the mesh within the swirler as long as the proper flow rate and swirling angles were correctly reproduced. To investigate this question, cA and cI were run on the fine mesh (Section 3) with both AVBP and YALES2.

The statistics of the fine mesh are time-averaged in AVBP and YALES2 during 13.5 t_{ref} (41 ms). Statistics have been checked to be converged. Mean and RMS of the axial and transverse velocity of configuration A are shown in Figure 8. For the sake of compactness, only the results at $x = 5.5$ mm are displayed since most discrepancies between LES and PIV appeared at this location. The configuration I is not shown but observations are similar.

Figure 8 shows that mesh refinement has a limited impact on the axial or traverse velocities, nor on the swirl velocity (not shown). The statistics obtained in the two LES codes are already spatially converged on the baseline mesh.

4.4. *Pressure losses*

The previous section has shown that mesh refinement did not affect velocity profiles significantly, suggesting that LES on the two meshes used here is sufficiently precise for this swirling flow. However, a different conclusion is obtained when considering pressure losses. A precise evaluation of pressure losses in swirlers is the first issue during the design of these systems. Typical pressure losses (normalized by the mean chamber pressure) in such systems vary from 3 to 8 percent and must be minimized to increase the engine efficiency. Table 4.4 summarizes the values of the normalized pressure losses obtained experimentally and numerically for configuration cA (similar conclusions are obtained for configuration cI). The experimental uncertainty indicated by experimentalists for the normalized pressure loss is $\pm$ 0.1 percent. All CFD predictions range from 8 to 10 percent showing that, unlike velocity profiles which are correctly captured, pressure losses are overestimated by CFD on these grids. Refining the grid from 8.6 to 43.7 and even 357 M cells in YALES2 leads only to a small improvement (from 10 to 8.6 percent). Using wall resolved LES in the swirler passages is obviously not realistic in terms of computational cost. RANS actually does slightly better with a prediction of 8 percent which is grid converged. Understanding what controls pressure losses in the swirler will

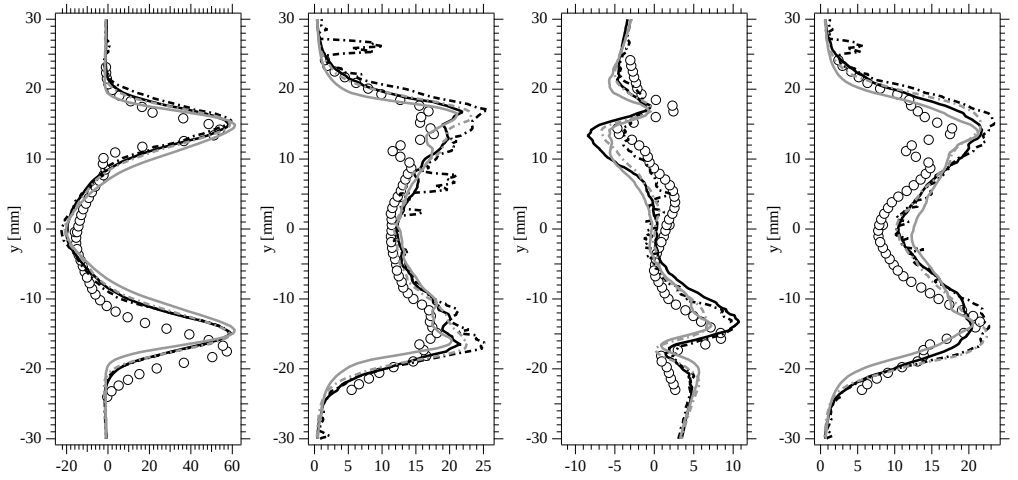

(a) u (m.s^{-1}) (b) u_{rms} m.s^{-1}) (c) v (m.s^{-1}) (d) v_{rms} m.s^{-1})

FIGURE 8. Mesh refinement study in AVBP and YALES2. Time-averaged mean (8(a) and 8(c)) and RMS (8(b) and 8(d)) of axial and azimuthal velocity profiles at $x = 5.5$ mm for configuration A. Comparison between the LES baseline mesh (———), LES finer mesh (-·-·-) and PIV (◯). Black and gray solid lines stand for AVBP and YALES2, respectively.

Method	Type	Mesh	SGS model	Normalized pressure loss
Experiment	Pressure sensors	N/A	N/A	6.6 ± 0.1
AVBP	LES - wall resolved	8.6 M cells	WALE	10.1
AVBP	LES - wall resolved	43.7 M cells	WALE	9.7
YALES2	LES - wall resolved	8.6 M cells	WALE	10.0
YALES2	LES - wall resolved	8.6 M cells	DYN. SMAG.	9.7
YALES2	LES - wall resolved	43.7 M cells	DYN. SMAG.	8.7
YALES2	LES - wall resolved	357 M cells	DYN. SMAG.	8.6
FLUENT	RANS - law of the wall	8.6 M cells	k-ε	8.14
FLUENT	RANS - law of the wall	43.7 M cells	k-ε	8.08

TABLE 2. Normalized pressure losses for configuration cA.

require a Uncertainty Quantification (UQ) study of this specific point, which was initiated with Fluent during the 2012 Summer Program. Preliminary results are shown in next section.

4.5. *Uncertainty quantification of the recirculation zone*

The good prediction of the central recirculation zone (CRZ) position is critical for the control of the pressure loss: the closer the CRZ of the swirler mouth, the higher the pressure loss. In this study, a presumed coflow speed has been arbitrarily set to one tenth of the inlet velocity ($u_{coflow} = 1.32$ m.s^{-1}). Consequently, a preliminary UQ study has been performed in order to account for the variability of this quantity of interest, which is so far an uncertain input. A flat distribution of the coflow speed between 1 and

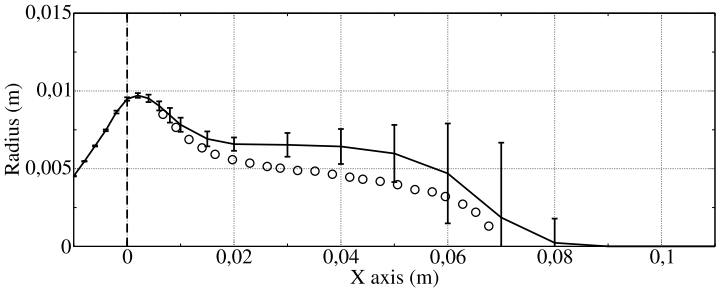

FIGURE 9. Statistical envelope of CRZ position at +/- 2 Sigma for Configuration A calculated with Fluent (———: mean / error bars : +/- 2 Sigma) and measures with PIV (◯). The vertical dashed line at $x = 0$ m refers to the swirler exit.

10 m.s^{-1} has been assumed and discretized in nine values with a tensor approach. This study has been performed with the Fluent code, on the 8 M cells mesh in order to have reasonable return times.

Figure 9 presents the mean position of the recirculation zone (isoline of zero axial velocity) with the +/- 2 Sigma interval in which the CRZ is located. The upstream position of the CRZ ($x > 0.03$ m) is the most sensitive to the coflow speed. Downstream ($x < 0.02$ m), the CRZ position does not vary and agrees fairly well with the experiments. Since the pressure loss is closely related to the downstream part of the CRZ, this UQ study shows that the prediction of this quantity is robust as a function of the coflow speed.

4.6. *Experimental and numerical study of unstable modes in cI and cA*

The analysis of averaged and RMS velocity fields in Section 4.1 to 4.3 showed a fairly good agreement between LES and experiment and similar mean flow fields for cA and cI, showing that the displacement of the flare holes seems to play a minor role on the mean flow. This section shows that even though they exhibit similar mean flows fields, configurations A and I exhibit different hydrodynamic modes and that LES captures these changes.

Experimentally, unstable modes in cA and cI were characterized using hot-wire measurements inside the swirler at point P1 (Figure 2). Figure 10(a) and 10(b) first show the velocity spectra at P1 for an increasing mass-flow rate for configuration A obtained experimentally and with AVBP respectively. LES velocity spectra correspond to a FFT of the axial velocity u. In order to reduce the signal-to-noise ratio and to account for the fact that the hot-wire probe has a finite length, spectra of twenty-seven probes around P1 ($\pm$1 mm) have been averaged. Two modes appear for cA and their frequencies increase with the mass flow rate, suggesting that these modes are hydrodynamical and follow a constant Strouhal scaling. LES (with AVBP on the baseline mesh) captures the two modes and predicts their evolution with the mass flow rate. The corresponding Strouhal number St_h can be defined using the bulk velocity (34 m/s) and the diameter of the swirler before the peripheral holes section (D=25 mm). The first mode corresponds to a Strouhal number of 0.64 while the second one corresponds to a Strouhal of 1.92 (Figure 11). The low-frequency mode frequency ($\mathrm{St}_h = 0.64$) is in the range of Strouhal numbers observed for PVCs in swirling flows.

LES frequencies reported in Figure 11 are larger than experimental values but mesh independency tests demonstrate that the LES frequencies converge to the experimental value when the mesh size increases: Figure 12(a) shows that the frequency of the second

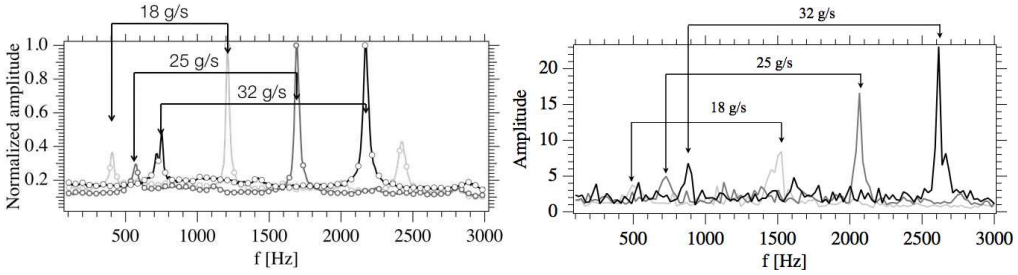

FIGURE 10. Effect of mass-flow rate on velocity spectra at probe P1 (Figure 2(a)): experiment (a) and AVBP (b). The unstable frequencies vary linearly with flow rate in both LES and experiment.

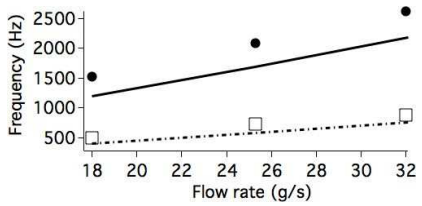

FIGURE 11. Frequencies of the low- and high-frequency hydrodynamic modes as a function of the mass-flow rate obtained experimentally and numerically. ———: experiment second mode, — - — : experiment first mode, •: AVBP second mode, □ : AVBP first mode.

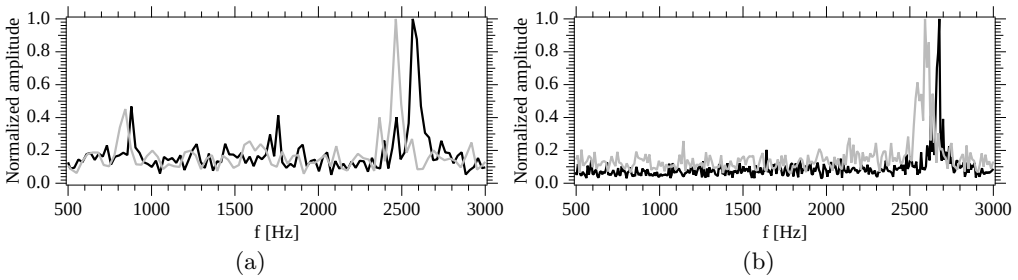

FIGURE 12. Impact of mesh refinement on LES results for cA: FFT of the hot wire velocity at P1 for AVBP (left) and YALES2 (right) on the baseline (———) and fine (———) mesh.

mode captured with AVBP goes from 2580 to 2450 Hz when the mesh is refined from 8.6 to 43.7 M cells (the experimental frequency is 2200 Hz for this regime). The trend is the same with YALES2.

Finally, configurations cA and cI are compared for the maximum flow rate (32 g/s): a major change is observed experimentally when the configuration is changed from cA to cI: the low frequency mode (around 800 Hz for a flow rate of 32 g/s) is strongly damped (Figure 13(a)). Results show that LES captures the fact that two modes appear in configuration A and only one in configuration I (Figure 13(b)). Interestingly enough, the first mode does not appear in cA with YALES2 (Figure 12(b)), even with the fine mesh. Note that it also does not appear with the very fine mesh of 357 M cells (not shown). Because YALES2 is a low Mach solver, this might suggest that the presence of the first mode of cA is related to a coupling between acoustics and hydrodynamics.

When the peripheral holes are displaced in cI compared to cA, the low-frequency mode

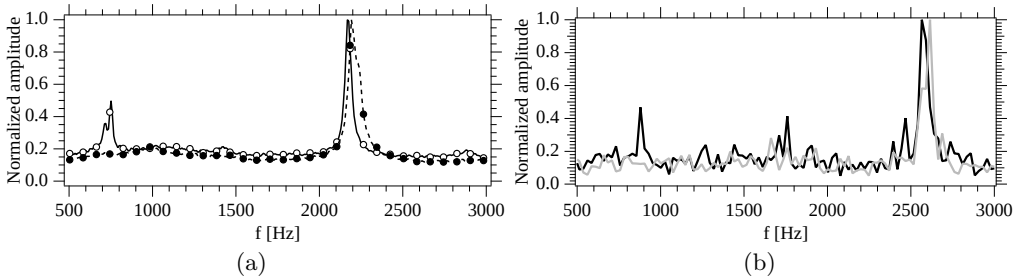

FIGURE 13. Spectra of hot wire velocity at P1 for configurations A and I. Left: Experimental data for cA (—◯—) and cI (– – •– –). Right: LES on the baseline mesh of cA (———) and cI (———).

disappears in LES with AVBP. The exact physical phenomenon leading to one mode at low frequency for cA is still under investigation and is beyond the scope of this proceeding. Nevertheless, this confirms that LES is indeed a proper tool to check whether a given swirler will produce strong hydrodynamic modes and how sensitive this mode will be to small design changes. Both incompressible (YALES2) and compressible (AVBP) solvers capture the second mode, associated to the PVC.

None of the RANS solvers provides any information on this point.

5. Conclusion

The present project focused on experimental and numerical studies of a swirling flow where small geometrical changes can lead to a variation of the natural hydrodynamic modes. Results show that RANS can be used to obtain pressure losses and mean velocity fields in this flow. LES capture both mean and turbulent fluctuations. Both compressible and incompressible LES solvers capture the hydrodynamic mode of the Precessing Vortex Core produced in the swirler. However, only the compressible LES can discriminate between two very similar swirler designs and show that one of them will exhibit a low frequency mode while the other does not.

Acknowledgments

The authors acknowledge the support of Dr T. Lederlin (TURBOMECA), Prof G. Iaccarino of CTR (Stanford) and the KIAI project coordinator Dr S. Roux (Snecma). The support of E. Motheau and Pr F. Nicoud for the acoustic computations is gratefully acknowledged.

REFERENCES

BILLANT, P., CHOMAZ, J.-M. & HUERRE, P. 1998 Experimental study of vortex breakdown in swirling jets. *J. Fluid Mech.* **376**, 183–219.

COLIN, O. & RUDGYARD, M. 2000 Development of high-order taylor-galerkin schemes for unsteady calculations. *J. Comput. Phys.* **162** (2), 338–371.

DELLENBACK, P., METZGER, D. & NEITZEL, G. 1988 Measurement in turbulent swirling flows through an abrupt axisymmetric expansion. *AIAA J.* **13** (4), 669–681.

EL-ASRAG, H. & MENON, S. 2007 Large eddy simulation of bluff-body stabilized swirling non-premixed flames. *Proc. Combust. Inst.* **31**, 1747–1754.

Granet, V., Vermorel, O., Lacour, C., Enaux, B., Duguè, V. & Poinsot, T. 2012 Large-Eddy Simulation and experimental study of cycle-to-cycle variations of stable and unstable operating points in a spark ignition engine. *Combust. Flame* **159** (4), 1562 – 1575.

Granet, V., Vermorel, O., Leonard, T., Gicquel, L., & Poinsot, T. 2010 Comparison of nonreflecting outlet boundary conditions for compressible solvers on unstructured grids. *AIAA J.* **48** (10), 2348–2364.

Gupta, A. K., Lilley, D. G. & Syred, N. 1984 *Swirl flows*. Abacus Press.

Ho, C. M. & Huerre, P. 1984 Perturbed free shear layers. *Ann. Rev. Fluid Mech.* **16**, 365–424.

Huang, Y., Sung, H. G., Hsieh, S. Y. & Yang, V. 2003 Large eddy simulation of combustion dynamics of lean-premixed swirl-stabilized combustor. *J. Prop. Power* **19** (5), 782–794.

Huang, Y., Wang, S. & Yang, V. 2006 Systematic analysis of lean-premixed swirl-stabilized combustion. *AIAA J.* **44** (724-740).

Huang, Y. & Yang, V. 2004 Bifurcation of flame structure in a lean premixed swirl-stabilized combustor: Transition from stable to unstable flame. *Combust. Flame* **136**, 383–389.

Launder, B. E. & Jones, W. P. 1972 The prediction of laminarisation with a two-equation model of turbulence. *International J. of Heat and Mass Transfer* **15**, 301–314.

Lefebvre, A. H. 1999 *Gas Turbines Combustion*. Taylor & Francis.

Mare, F. D., Jones, W. P. & Menzies, K. 2004 Large eddy simulation of a model gas turbine combustor. *Combust. Flame* **137**, 278–295.

Moureau, V., Domingo, P. & Vervisch, L. 2011 From large-eddy simulation to direct numerical simulation of a lean premixed swirl flame: Filtered laminar flame-pdf modeling. *Combust. Flame* **158** (7), 1340–1357.

Nicoud, F. & Ducros, F. 1999 Subgrid-scale stress modelling based on the square of the velocity gradient. *Flow, Turb. and Combustion* **62** (3), 183–200.

Poinsot, T. & Lele, S. 1992 Boundary conditions for direct simulations of compressible viscous flows. *J. Comput. Phys.* **101** (1), 104–129.

Poinsot, T. & Veynante, D. 2011 *Theoretical and Numerical Combustion*. Third Edition (www.cerfacs.fr/elearning).

Roux, S., Lartigue, G., Poinsot, T., Meier, U. & Bérat, C. 2005 Studies of mean and unsteady flow in a swirled combustor using experiments, acoustic analysis and large eddy simulations. *Combust. Flame* **141**, 40–54.

Selle, L., Lartigue, G., Poinsot, T., Koch, R., Schildmacher, K.-U., Krebs, W., Prade, B., Kaufmann, P. & Veynante, D. 2004 Compressible large-eddy simulation of turbulent combustion in complex geometry on unstructured meshes. *Combust. Flame* **137** (4), 489–505.

Shih, T.-H., Liou, W. W., Shabbir, A., Yang, Z. & Zhu, J. 1995 A new k-ϵ eddy viscosity model for high reynolds number turbulent flows. *Computers & Fluids* **24** (3), 227 – 238.

Staffelbach, G., Gicquel, L., Boudier, G. & Poinsot, T. 2009 Large eddy simulation of self-excited azimuthal modes in annular combustors. *Proc. Combust. Inst.* **32**, 2909–2916.

Syred, N. 2006 A review of oscillations mechanisms and the role of the precessing vortex core (pvc) in swirl combustion systems. *Prog. Energy Comb. Sci.* **32**, 93–161.

Vanierschot, M. & den Bulck, E. V. 2007 Hysteresis in flow patterns in annular swirling jets. *Experimental Thermal and Fluid Science* **31** (6), 513–524.

Wang, S., Yang, V., Hsiao, G., Hsieh, S.-Y. & Mongia, H. C. 2007 Large-eddy simulations of gas-turbine swirl injector flow dynamics. *J. Fluid Mech.* **583**, 99–122.

Wolf, P., Balakrishnan, R., Staffelbach, G., Gicquel, L. & Poinsot, T. 2012 Using LES to study reacting flows and instabilities in annular combustion chambers. *Flow, Turb. and Combustion* **88**, 191–206, 10.1007/s10494-011-9367-7.